

# Continuous Crystallization in a Helically-Coiled Flow Tube: Analysis of Flow Field, Residence Time Behavior and Crystal Growth

*Viktoria Wiedmeyer,<sup>a\*</sup> Felix Anker,<sup>b</sup> Clemens Bartsch,<sup>b</sup> Andreas Voigt,<sup>a</sup> Volker John,<sup>b,c</sup> Kai Sundmacher<sup>a,d</sup>*

<sup>a</sup> Otto-von-Guericke-University Magdeburg, Department Process Systems Engineering, Universitätsplatz 2, D-39106 Magdeburg, Germany

<sup>b</sup> Weierstrass Institute for Applied Analysis and Stochastics, Leibniz Institute in Forschungsverbund Berlin e. V. (WIAS), Mohrenstr. 39, D-10117 Berlin, Germany

<sup>c</sup> Free University of Berlin, Department of Mathematics and Computer Science, Arnimallee 6, D-14195 Berlin, Germany

<sup>d</sup> Max Planck Institute for Dynamics of Complex Technical Systems, Department Process Systems Engineering, Sandtorstr.1, D-39106 Magdeburg, Germany

\* [viktoria.wiedmeyer@ovgu.de](mailto:viktoria.wiedmeyer@ovgu.de)

## **ABSTRACT**

A continuously operated helically-coiled flow tube (HCT) crystallizer is investigated for crystal growth. Inline video-imaging is used for crystal shape analysis and residence time estimation of potash alum. The main finding is that there is a size-dependent particle residence time. Large particles are moving faster through the HCT than small particles. Consequently, small crystals have more time to grow in the HCT. Physical reasons for this behavior are proposed e.g. small-scale flow characteristics. In a direct numerical simulation of the instationary Navier-Stokes equations, velocity fluctuations and a secondary flow are identified. The presented flow field may have a different impact on the particles and cause the size-dependent particle residence time. A particle-size dependent residence time may potentially narrow the crystal size and shape distribution in such a process, frequently a desired feature in solids' production.

## **1. INTRODUCTION**

Crystallization is a fundamental part for a large number of active pharmaceutical ingredient (API) production processes for purification.<sup>1</sup> A common subsequent step is filtration. Small crystals, flakes and easily breakable elongated crystals should be avoided to prevent filter clogging.<sup>2</sup> In downstream processing operations, a narrow crystal size and shape distribution (CSSD) is often desired. A compact crystal population with a narrow CSSD improves the ability of the material to flow which is important in animal feedstuff handling<sup>3</sup> and avoids caking during storage.<sup>4,5</sup> Furthermore, crystal shape is a property that is significant to be controlled since it determines crystal properties as surface area and thus bioavailability<sup>6</sup> of APIs or in other cases the size of the reactive face areas of catalysts.<sup>7</sup>

Crystals are produced in both batch and continuous process configurations. An overview of the crystallizer types is given in the following. The configurations are judged by their potential to produce crystal populations with a narrow CSSD. According to ter Horst et al.,<sup>1</sup> continuous crystallization research focuses currently on mixed-suspension, mixed-product-removal (MSMPR) crystallizers, on MSMPR cascades and on tubular crystallizers, for instance straight tubes, coiled flow inverters (CFIs), helically-coiled flow tubes (HCTs) and oscillatory baffled crystallizers. In industrial production, the traditional operation mode is batch crystallization.<sup>6</sup> Batch crystallizers are used for small-scale operations, either when materials are frequently changed or when they are difficult to handle due to high viscosities or due to a tendency to encrust. There are some limitations to the application of batch crystallizers. Considering scale-up, cooling is difficult and inhomogeneities increase. On the one hand, stirring needs to be increased to improve homogeneity; on the other hand, stirring should be low to avoid breakage<sup>6</sup> and to avoid a broadening of the CSSD. In contrast to batch-to-batch-variability, constant product quality can be reached in continuous crystallization at steady state.<sup>8</sup> Furthermore, there is interest in applying continuous crystallizers to pharmaceutical process chains. Further batch operation problems can be eliminated, such as down times, contamination risks and costs due to decanting.<sup>9</sup>

The continuous MSMPR crystallizer overcomes batch-to-batch-variability and contamination problems. A remaining disadvantage of the MSMPR crystallizer is the broad crystal residence time distribution (RTD) and thus the broadening of the CSSD. For large-scale MSMPR crystallizers cooling is still difficult. A cascade of MSMPR crystallizers can be implemented<sup>10</sup> to improve cooling capacity, to reduce inhomogeneities and to narrow the RTD. The crystal RTD narrows with the number of MSMPR crystallizers and approaches a plug flow but, in practice,

only a few MSMPRs are used to minimize equipment costs. An additional method to approach plug flow are tubular crystallizers. In tubular configurations, quick cooling is possible due to a high surface to volume ratio while there is no stirring.

There are different process configurations of tubes. In straight tubes, narrow RTDs can be reached by an increase in mixing at high fluid velocities and at turbulent conditions.<sup>1</sup> When high velocities are applied, residence times are low. Hence, tube length has to increase to realize a desired growth. This is usually limited for practical reasons. An additional method to increase mixing is coiling<sup>11</sup> which is typically realized by HCTs or by CFIs.<sup>12,13</sup> In this study, a tubular crystallizer is considered to enable crystal production in a process chain and to achieve a narrow RTD. Although the CFI leads to a potentially narrower CSSD,<sup>11</sup> the HCT setup is more flexible when its geometry is changed and it can be considered as a basic subunit of the CFI. Consequently, the aim of this work is to characterize the HCT crystallizer with respect to the RTD and the achievable CSSD for growth-dominated crystallization processes.

HCTs have already been applied in several fields,<sup>14</sup> e.g. for liquid-liquid mixing<sup>14,15</sup> or for heat exchanging<sup>14,16,17</sup> due to their mixing properties and high heat transfer rates. The HCT is relatively new to the field of crystallization since tubular crystallizers are subject to the risk of clogging.<sup>18</sup> Clogging can be caused by crystal sedimentation which can be avoided by an increase in fluid velocity or by an increase in turbulence which is realized by oscillatory baffled crystallizers.<sup>19,20</sup> Furthermore, crystals can grow at thermal bridges.<sup>21</sup> Thus, metal sensors should be avoided. Additionally, high suspension densities increase the risk of tube blocking. Consequently, uncontrolled nucleation is avoided by different continuous seeding strategies in the literature.<sup>12,13,18,22</sup> First studies applying the HCT for API coating and crystal growth were published by Khinast and co-workers.<sup>18,23,24,25,26,27</sup> A sonicated tubular crystallizer was designed

by Furuta et al.<sup>22</sup> The HCT has not yet been investigated for crystal shape control although the shape strongly determines API efficacy<sup>6</sup> as well as downstream processing.<sup>2</sup>

Therefore, the objective of this work is to apply methods for shape control to the continuous HCT crystallizer to grow crystals with a narrow CSSD. The HCT is operated as a cooling crystallizer in a growth-dominated regime. For example, crystal shape control can be realized by anti-solvent crystallization. Since crystallization is usually applied for purification, the use of an anti-solvent would necessitate an additional step in the downstream process chain to remove the anti-solvent again from the produced crystals. To avoid this step, potash alum seed crystals are added to an aqueous potash alum solution. Potash alum crystallizes as potassium aluminum sulfate dodecahydrate which is a compound that contains water molecules within the crystal. It crystallizes predominantly as an octahedron under the applied process conditions.<sup>28</sup> Hence, its shape can be described with one internal size coordinate  $h$  which is the perpendicular distance of the crystallographic faces to the crystal center. The crystals are recorded by means of video imaging at the HCT outlet. The 3D crystal shape is estimated from the recorded 2D projections applying algorithms presented by Borchert et al.<sup>29</sup> for bivariate crystal populations.

The CSSD of the crystal population at the HCT outlet is influenced by the crystal RTD. Therefore, at first, the RTD of the HCT setup was characterized in this study. Experiments have shown that the crystals have a size-dependent residence time in the HCT for laminar Reynolds numbers. Large crystals were faster and had a shorter residence time. A size-dependent residence time has already been reported for experiments with spherical particles in a straight tube<sup>30</sup> and for experiments with elastic fibers in a HCT<sup>31</sup> but not yet for crystals in the HCT.

Baptista et al.<sup>30</sup> have observed that large particles show a higher normalized linear velocity than small particles in straight tubes. They used tubes four to nine times as large as in this work and particles with a higher particle to tube diameter ratio. They contributed the effect to higher drag forces for larger particles. A result of their work is that particle density and fluid velocity have a higher effect on the linear particle velocity. Therefore, succeeding articles investigating the residence time in helical tubes, e.g. by Palazoglu and Sandeep,<sup>32</sup> focus mainly on these two parameters.

Redlinger-Pohn et al.<sup>31</sup> investigated the fiber RTD by means of experiments and CFD-DEM simulations. In the simulations, large long particles and smaller short particles had similar residence times. The experimentally observed shorter residence time for large long fibers was contributed to flocculation. Flocculation does not happen for compact crystals. Thus, further research is necessary for compact crystals with different sizes which is the focus of this work.

Tiwari et al.<sup>33</sup> analyzed a HCT setup in CFD simulations for spherical particles of a few  $\mu\text{m}$  in diameter at low Reynolds numbers. The investigated Dean numbers ranged from 50 to 1000, while the Dean numbers in this work, 293 and 417 for the Reynolds numbers given in Subsection 3.4, lie in the same range. In the setup of Tiwari et al.,<sup>33</sup> most particles were located at the inner bend of the tube since the shear force due to secondary flow points towards the inner bend. Furthermore, they stated that the secondary flow helps in distributing particles in the cross section where the distribution gets more uniform with decreasing particle size and increasing Dean number. In the present work, simulations showed that similar Dean vortices are found. Consequently, the small flow characteristics may also affect particles differently depending on their size in our setup.

This study is structured as follows: Section 2 presents the experimental setup, Section 3 introduces the experimental results under varying process conditions. Hypotheses are proposed to explain the size-based separation in the measured RTD. With the purpose of analyzing the RTD, velocity profiles are shown for the given HCT setup. The profiles are obtained by a direct numerical simulation for a laminar time-dependent flow. Section 4 concludes this article.

## 2. MATERIALS AND METHODS

**2.1 Materials.** Potassium alum dodecahydrate purchased from Merck (CAS No. 7784-24-9, assay 99.0 to 100.5%) represents the model substance in this work. The solvent is deionized water. The solubility of potash alum was determined in the range of 20-50 °C and is shown in Figure S1 of the Supporting Information. The mass fraction  $w$  is given in kg of hydrate/kg of added free water. An empirical quadratic polynomial model fit describes the temperature dependence of the equilibrium concentration

$$w_{\text{eq}}(\theta) = 0.180 \times 10^{-3}\theta^2 - 4.392 \times 10^{-3}\theta + 0.131 \quad (1)$$

where  $\theta$  is the temperature in °C. The coefficient of multiple determination is 0.9991. The resulting model mass fractions deviate by a maximum of 3.6% from measurements of Mullin et al.<sup>34</sup> The relative supersaturation  $S$  is defined as

$$S(\theta) = \frac{w}{w_{\text{eq}}(\theta)}. \quad (2)$$

**2.2 Imaging Methods.** Following de Albuquerque et al.,<sup>35</sup> imaging is the state of the art method to estimate particle size and shape at low suspension densities. Here, the crystal shape is estimated by inline video-imaging as presented by Borchert et al.<sup>29</sup> The algorithms were

extended by a potash alum crystal database. The database was generated for octahedra of varying orientation and size. The crystal shape is characterized by the perpendicular distance  $h$  of the crystal faces to the crystal center,<sup>36,37</sup> called H-representation and is shown in Figure 1. Assuming that only octahedral faces occur,  $h$  is a scalar and the CSSD is univariate. Whether the octahedral steady state shape<sup>38</sup> is reached depends on the initial shape of the seeds and on the residence time. Potash alum crystals can develop octahedral faces {111}, cubic faces {100}, rhombic-dodecahedral faces {110} and combinations thereof. Three further faces could in principle appear.<sup>28</sup> Under the conditions called “rapid cooling” by Buckley<sup>28</sup> which are applied in this work, potash alum crystallizes as octahedron. In rare cases, the octahedron is predominant with cube faces just appearing.<sup>28</sup>

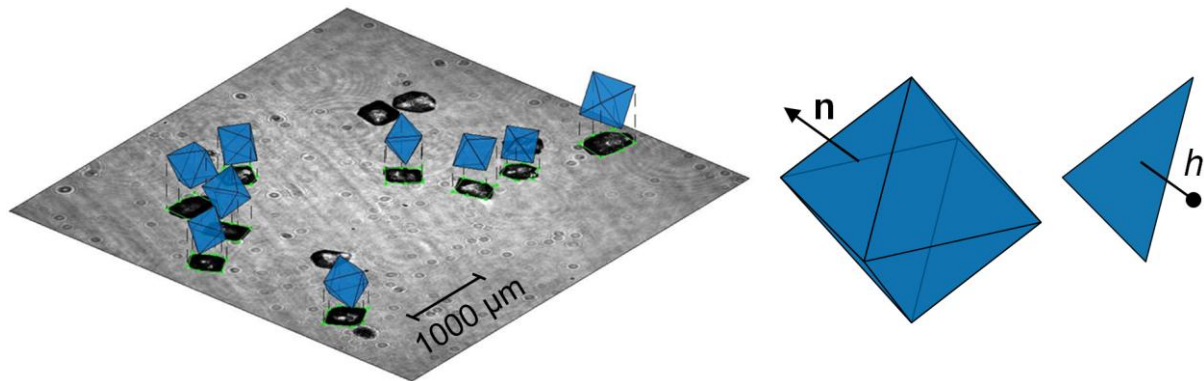


**Figure 1.** During an experiment, particles are imaged by the flow-through microscope. In the left part, potash alum crystals are depicted as dark objects in a grayscale image. The estimated crystal shapes are shown as blue octahedra above the dark objects. The right part illustrates the normal vector  $\mathbf{n}$  of an octahedral face and the perpendicular distance  $h$  from the crystal face to the crystal center.

Low suspension densities and a small cell width enable a measurement of single objects as indicated in Figure 1. The crystals are visible as black objects in the projection. The estimated

shape is depicted as blue octahedron above each detected single crystal in Figure 1. For shape estimation, a boundary curve of the projection is compared with boundary curves of a database to estimate the original orientation and shape of the projected crystal as shown by Borchert et al.<sup>29</sup> Objects identified as bubbles, aggregates or nuclei are not considered in the shape estimation. Small objects with a projection area smaller than 556 pixels and consequently with an equivalent circular diameter smaller than 80  $\mu\text{m}$  are withdrawn since the number of pixels is too small to estimate whether the object is an agglomerate or a single crystal. The characteristic size  $h$  of an octahedron with a projection area of 556 pixels depends on the octahedron's orientation: assuming exemplarily that the projection is a square with an edge length equal to the octahedron edge length,  $h$  is about 26  $\mu\text{m}$ ; when the midplane is perpendicular to the projection plane,  $h$  is about 30  $\mu\text{m}$ .

**2.3 Seed Crystals.** To generate seed fractions, potash alum (see Subsection 2.1) was dry sieved for 60 min with a vibratory sieve shaker (AS 200 control, Retsch) using meshes of 150, 200, 212, 300 and 400  $\mu\text{m}$ . Following Mullin,<sup>8</sup> potash alum has an average Vickers hardness compared to other crystalline substances whereas Girolami and Rousseau<sup>39</sup> mention that sieve wires can deform the crystals and dislocations can already exist prior to delivery. Therefore, growth dispersion may increase.

For each size fraction, the number density distribution was measured in preliminary experiments. The experiments were carried out in anti-solvent ethanol<sup>40</sup> to avoid shape changes. The estimated initial number density distributions are shown in Figure 2 for one experiment of each fraction. All experiments were repeated and the repetitions showed similar number densities. In Figure 2, the fractions are labeled by A to D with increasing sieve mesh size, as stated in the beginning of this subsection. The fractions overlap due to a limited selectivity of

sieving and due to the existence of elongated initial crystals. The graph A+D shows a mixture of 111 mg of the smallest and 257 mg of the largest size fraction. The minimal sizes  $h$  of the sieved size fractions were determined as 40  $\mu\text{m}$  for A, 45  $\mu\text{m}$  for B, 50  $\mu\text{m}$  for C, 100  $\mu\text{m}$  for D and 40  $\mu\text{m}$  for the fraction mixed of the smallest seed fraction and the largest one. Crystals smaller than the particular minimal size were not included in the image analysis in order to separate potential nuclei from the seed fraction.

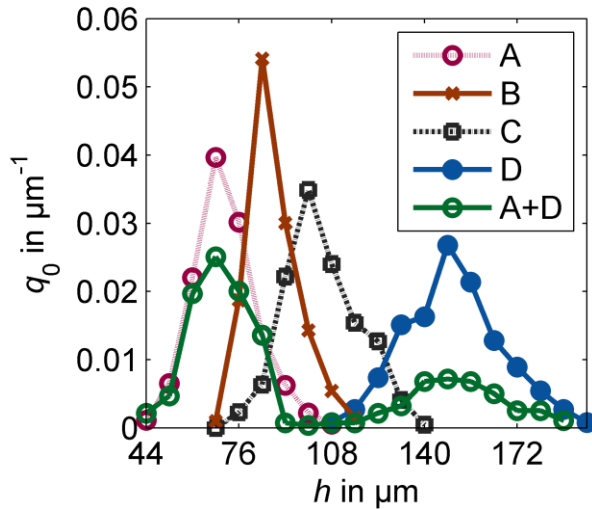


**Figure 2.** Number density distribution of the initial seed fractions over the perpendicular distance of the crystal faces to the crystal center  $h$ . At the beginning and the end of each curve only one value smaller than 0.002 is shown.

**2.4 Setup.** The experiments were performed in a continuously operated HCT crystallizer. The setup is illustrated in Figure 3. The components are: (1) reservoir, (2) pump, (3) debubbler, (4) three-way valve for seed addition, (5) HCT and (6) flow-through microscope. They are connected by polysiloxane tubes with an inner diameter ( $d_i$ ) of 0.006 m and an outer diameter of 0.009 m as shown in Figure 4. The tube has a length ( $L$ ) of 34 m from position (4) to (6). The

coil diameter ( $d_c$ ) at the tube center is 0.1145 m. Hence, the curvature  $\kappa$  is the ratio of  $d_i$  to  $d_c$  and equals 0.052.

The coils are in contact with each other; thus the pitch distance  $p$  equals the outer tube diameter of 0.009 m. The vertical HCT was operated in two different modes: upwards coiling in which the inlet is at the bottom of the vertical HCT and downwards coiling in which the inlet is at the top of the vertical HCT. For upwards/downwards coiling, the segment between the seed addition (4) and the HCT inlet (5) has a length of 2.0 m (upward) or 1.3 m (downward). The distance from the HCT outlet (5) to the flow-through microscope (6) is 2.8 m (upward) or 3.8 m (downward). The suspension in the 5 L reservoir is agitated by a diagonal 4-blade stirrer operated at a speed of 200 rpm. A gear pump (4030-280-DM, Pumpenfabrik Ernst Scherzinger) is used to pump fresh solution through a woven wire mesh filter of aperture width 170  $\mu\text{m}$  from the reservoir to the HCT. A Coriolis type direct mass flow sensor (CORI-FLOW, Bronkhorst) is located between the reservoir (1) and the pump (2) to measure the current mass flow. The debubbler at position (3) does not affect the crystals, which are inserted behind the hold-up at position (4) in the experiments.

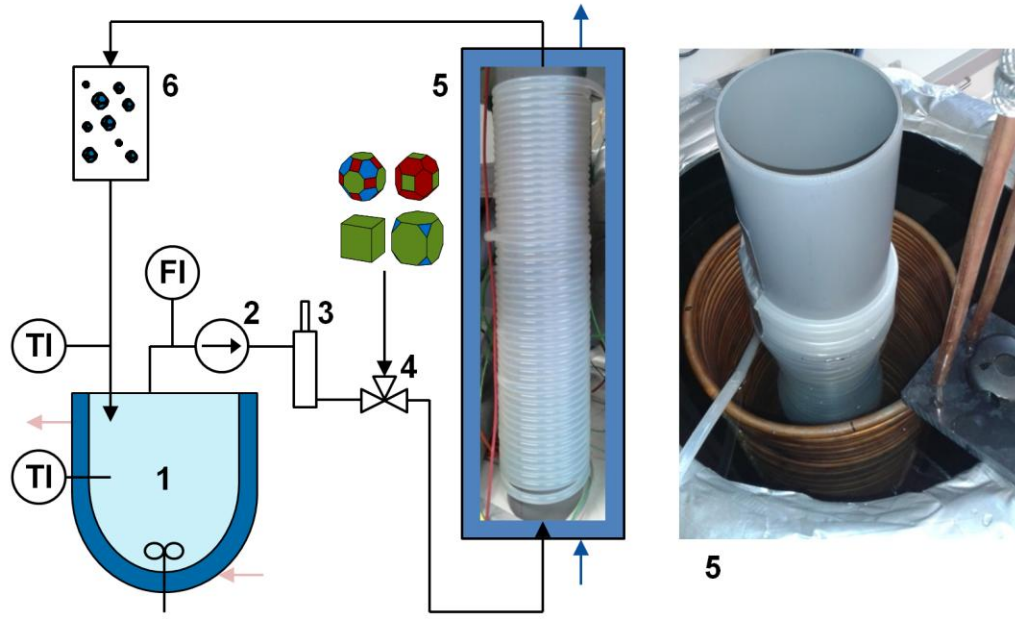


**Figure 3.** HCT crystallizer configuration with (1) reservoir, (2) pump, (3) debubbler, (4) three-way valve for seed addition, (5) HCT cooled by a cooling bath which is equipped with copper cooling coils and (6) flow-through microscope.

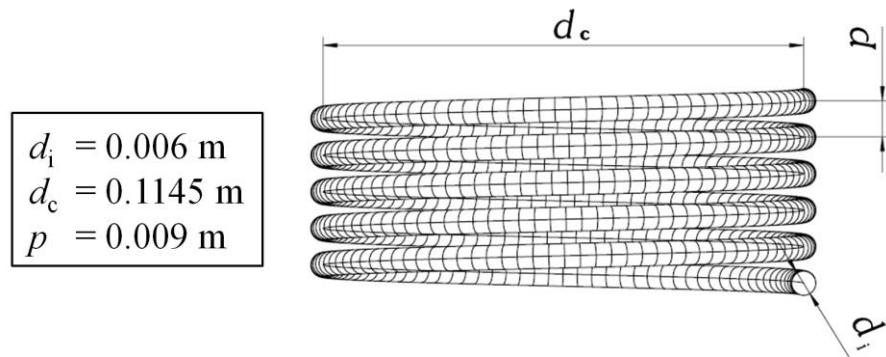


**Figure 4.** HCT design illustrated for five coils with dimensioning: inner tube diameter  $d_i$ , coil diameter  $d_c$  and pitch distance  $p$ .

Different methods can be applied to cool the HCT, e.g. air cooling,<sup>11</sup> segmented jackets<sup>41</sup> and cooling baths.<sup>23</sup> In this study, a (5) cooling bath is chosen. The cooling conditions are well-defined since the outer cooling temperature and thus the thermal transmittance is approximately

constant along the HCT. The cooling bath has a water volume of 200 L. Water is cooled with a (5) coiled copper heat exchanger which is connected to a thermostat (F32, Julabo). The copper heat exchanger with a diameter of 0.24 m is immersed in the cooling bath and located around the HCT. The plastic cooling bath is isolated with wool and aluminum foil on the side and with floating pellets at the top to establish a constant cooling bath temperature. Gas bubbles are used to increase mixing in the cooling bath. There is a temperature difference of about 1 °C in the cooling water at operation conditions, with a higher temperature at the top.

With the intention of characterizing the residence time and the CSSD of the crystal population, the HCT outlet is equipped with a video flow-through microscope (Qicpic, Sympatec). The suspension passes a flow-cell of 0.002 m width with a field of view of 0.005 m × 0.005 m. Behind the Qicpic, in the tube outlet, the HCT outlet temperature is monitored by a type K thermocouple. Finally, the suspension is flowing back into the double-jacketed reservoir. To ensure dissolution of the crystals, the reservoir temperature is always kept 1 to 2 °C above saturation temperature. The temperature in the reservoir is measured using a PT100 thermocouple. The double-jacket of the reservoir is controlled by a thermostat (FP40, Julabo).

**2.5 Experimental Procedures.** In the following, all experiments described have been carried out in the setup which was previously presented. All experiments were conducted for upwards and downwards coiling of the HCT. The debubbler was implemented in all experiments except in the residence time measurements of the continuous phase in upwards coiling mode. The effect of the debubbler is discussed in Subsection 3.1.

The residence time and the dispersion of the fluid were determined for the relevant segment of the tube in which the crystals grow. The segment is located between position (4) and (6) in

Figure 3. The residence time of the continuous phase was measured with a conductivity probe (FYA641LFP1, measurement range from 0.001 to 2 S/m, Ahlborn). The conductivity was recorded every 0.6 s. The probe is an active probe with automatic temperature compensation. Since large amounts of water were required for the experiments and the probe was equipped with an automatic temperature correction, the fluid temperatures were not identical for the experiments but ranged from 22 to 27 °C. Initially, water was pumped from the reservoir through the HCT. Next, the inlet was switched with a three-way valve to a potash alum solution ( $w$  was set to 70 g of hydrate/kg of free water) from a separate laboratory flask and back to water. The solution in the flask was prepared at least one day before each experiment to allow dissolution of the potash alum solute in water. The conductivity probe was located at position (6). Four different mean fluid velocities were applied by adjustment of the pump speed. The measurements were repeated at position (4) to determine the corresponding inlet signal. Additionally, the average mass flow rates of water and potash alum solution were determined by weighing measurements for 30 s to 2 min.

For the dispersed phase, all experiments were carried out at two fluid velocities. The corresponding average fluid velocities of the potash alum solution were determined by weighing measurements and averaged out to 0.24 m/s and 0.35 m/s. In the reservoir, 5 L of crystal-free solution was prepared. Prior to each set of experiments, the HCT was cleaned with water. Although the water in the HCT was removed with pressurized air, the remaining water slightly reduced the concentration and thus the saturation temperature of the solution decreased. The water amounted to a few percent of the reservoir content. During the experiments, samples were collected from the reservoir and air dried for two days to determine the concentration of the solution. The saturation temperature was between 38 and 41 °C for the isothermal experiments

and between 40 and 41 °C for the growth experiments. Prior to the start of an experiment, the solution was pumped through the system until a constant temperature profile was reached. At the beginning of each experiment, a dry inlet seed crystal population (see Subsection 2.3) was added to the free nozzle of the T-bore three-way valve (at position (4) in Figure 3). Defined amounts of seed crystals, namely 100-250 mg, were inserted. The nozzle containing the seeds was closed with a silicone plug and it was turned upwards such that the crystals fell down when the port was open. The valve was turned for 10 s such that all parts were open and the solution from the reservoir flushed the seed nozzle. The closed valve was rinsed immediately with water to avoid crystallization of the drying solution. The nozzle has a volume of about  $1.1 \times 10^{-6} \text{ m}^3$  where the plug occupies about  $0.3 \times 10^{-6} \text{ m}^3$ . Since the debubbler is located in front of the seed addition valve, a small amount of air from the nozzle can reach the HCT, but the air volume of the nozzle amounts only to about 0.08% of the HCT volume. During the whole process, the crystal population was recorded at the HCT outlet in grayscale videos at 10 Hz. First, the residence time of potash alum crystals was determined in i) isothermal experiments without growth and ii) growth experiments. To avoid clogging in the growth experiments, nucleation and thus a large supersaturation have to be avoided. Barrett and Glennon<sup>42</sup> determined the metastable zone width of potash alum for cooling rates between 0.2 and 0.7 °C/min at the saturation temperature of 40 °C. The conditions applied in the present work lie in this range. The metastable zone width determined by Barrett and Glennon<sup>42</sup> was between 4 and 8 °C. In the present study, the solution in the HCT reaches the lowest temperature at the HCT outlet. The concentration in the reservoir equals the HCT inlet concentration. Consequently, the solution at the HCT outlet was maintained to be never colder than 5 °C below the reservoir saturation temperature in the growth experiments to avoid nucleation.

**2.6 HCT Model Geometry for Flow Field Simulation.** Insight into the flow profile is achieved by means of a direct numerical simulation (DNS) of the flow, with a finite element approximation to the solution of the full instationary Navier-Stokes equations in a coiled tube geometry. This geometry should capture the characteristics of the experimental HCT crystallizer setup. There, the coiling of the tube is the distinct geometrical feature, which is to a large extent responsible for the flow characteristics and must thus be kept. However, since the DNS of the full Navier-Stokes equations is computationally out of reach for the entire coiled tube crystallizer of more than 30 m length, concessions have to be made.

Therefore, the model geometry contains just two coils in which the flow was simulated as illustrated in Figure 5. Preliminary studies with five coils in ParMooN<sup>43</sup> indicated that the main characteristics of the flow field develop already in a relatively small setup with just two coils, and there it can be computed within reasonable time.



**Figure 5.** Left: The computational domain for the simulation of the flow in a coiled tube is depicted with the inflow piece at the bottom of the picture. A cut plane is marked in the second coil. Right: The computational grid contains tetrahedral mesh cells.

The geometry for the flow simulation is the setup shown in Figure 5. It is a tube of 0.006 m inner diameter coiled up in two circular coils, the circle having a diameter of 0.111 m at the inner

wall of the tube. At the beginning and the end of the coiled part, straight inflow and outflow pieces are added. The length of the inflow piece at the tube bottom is 0.05 m. The outflow length is chosen to be 0.2 m. The vertical distance between the coils is 0.003 m, which results from the wall thickness of the tube in the experiment. This geometric setup is considered as a detail of the full experimental setup, which sufficiently captures its characteristics and is computationally feasible.

To define a computational grid, the two coils are subdivided into 360 small straight pieces each. These pieces are uniformly filled with stretched tetrahedral mesh cells, where each piece contains 1538 such cells, aligned in main flow direction. The inflow piece consists of 20 of such pieces, the outflow piece of 80. This equates to a total of 1,259,520 tetrahedral mesh cells.

**2.7 Numerical and Computational Methods for Flow Field Simulation.** Computing an approximate solution of the instationary Navier-Stokes equations is a challenging task which demands a well-tuned set of numerical and computational instruments. On a relatively complicated domain as depicted in Figure 5, the finite element method (FEM) offers an adequate and well-established framework.

In the following, the time-dependent incompressible Navier-Stokes equations are given. Let  $\Omega$  be a bounded domain in  $\mathbb{R}^3$ , and the final time  $T \in \mathbb{R}$ ,  $T > 0$ . The equations in nondimensionalized form read:

$$\begin{aligned}\partial_t \mathbf{u} - \nu \Delta \mathbf{u} + (\mathbf{u} \cdot \nabla) \mathbf{u} + \nabla p &= \mathbf{0} && \text{in } (0, T] \times \Omega \\ \nabla \cdot \mathbf{u} &= 0 && \text{in } (0, T] \times \Omega.\end{aligned}\tag{3}$$

The unknown functions  $\mathbf{u}$  and  $p$  are fluid velocity and pressure, respectively. While the fluid velocity is the target quantity, the pressure acts as a Lagrangian multiplier for the mass balance

equation. The time-dependent incompressible Navier-Stokes equations are capable of describing the full flow field, but their mathematical analysis and numerical analysis are challenging. For a state-of-the-art overview see John.<sup>44</sup>

With the purpose of finding a numerical solution, Equations 3 are first discretized in time. A popular choice is the second order accurate Crank-Nicolson time stepping scheme. Discretization in space is performed by the Galerkin finite element discretization. Choosing a pair of finite element spaces ( $V_h, Q_h$ ) leads to the following fully discrete system of Navier-Stokes equations. The discretized system is marked by the index  $h$ . At time step  $n + 1$ , with time step length  $\Delta t$ , functions  $(\mathbf{u}_h^{n+1}, p_h^{n+1}) \in (V_h, Q_h)$  that solve the following nonlinear system of equations have to be found

$$(\mathbf{u}_h^{n+1}, \mathbf{v}_h) + \frac{1}{2} \Delta t \left[ \nu (\nabla \mathbf{u}_h^{n+1}, \nabla \mathbf{v}_h) + ((\mathbf{u}_h^{n+1} \cdot \nabla) \mathbf{u}_h^{n+1}, \mathbf{v}_h) \right] - (\nabla \cdot \mathbf{v}_h, p_h^{n+1}) = (\mathbf{u}_h^{n+1}, \mathbf{v}_h) - \frac{1}{2} \Delta t \left[ \nu (\nabla \mathbf{u}_h^n, \nabla \mathbf{v}_h) + ((\mathbf{u}_h^n \cdot \nabla) \mathbf{u}_h^n, \mathbf{v}_h) \right] \quad (4a)$$

$$\Delta t (\nabla \cdot \mathbf{u}_h^{n+1}, q_h) = 0 \quad (4b)$$

for all test functions  $(\mathbf{v}_h, q_h) \in (V_h, Q_h)$ . A common approach consists in applying either Picard or Newton iteration to treat the nonlinear convective term  $((\mathbf{u}_h^{n+1} \cdot \nabla) \mathbf{u}_h^{n+1}, \mathbf{v}_h)$ . This approach requires the solution of multiple linear systems of equations per time step. An alternative is the class of IMEX (implicit-explicit) time-stepping schemes, which results in only one linear problem per time step. From this class of methods the linearly extrapolated Crank-Nicolson (CNLE(stab)) method is employed as proposed by Ingram.<sup>45</sup> The scheme replaces the “wind” in the convective terms of Equation 4a with a linear extrapolation from the solutions of the past two

time steps. In a formulation of CNLE(stab) proposed by John,<sup>44</sup> the convective term  $((\mathbf{u}_h^{n+1} \cdot \nabla) \mathbf{u}_h^{n+1}, \mathbf{v}_h)$  on the left-hand side of the Equation 4a is replaced with

$$\left( ((2\mathbf{u}_h^n - \mathbf{u}_h^{n-1}) \cdot \nabla) \mathbf{u}_h^{n+1}, \mathbf{v}_h \right) \quad (5)$$

and the convective term  $((\mathbf{u}_h^n \cdot \nabla) \mathbf{u}_h^n, \mathbf{v}_h^n)$  on the right-hand side of the Equation 4a is replaced with

$$\left( ((2\mathbf{u}_h^{n-1} - \mathbf{u}_h^{n-2}) \cdot \nabla) \mathbf{u}_h^n, \mathbf{v}_h \right). \quad (6)$$

This way, a linear scheme has been obtained. Its stability has been proven without a limitation on the time step size by Ingram.<sup>45</sup> Its implementation into an existing finite element code is rather simple.

An initial condition from the experiments is unknown and  $\mathbf{u}(t = 0)$  is set zero. At the inflow boundary, a Hagen-Poiseuille profile of 0.509 m/s central inflow velocity magnitude which is constant over time is prescribed. A volumetric flux of  $7.2 \times 10^{-6}$  m<sup>3</sup>/s is assumed. To avoid an impulsive start, the inflow is raised linearly over the first 0.1 seconds until it reaches the prescribed value. This approach compensates for the lack of an initial condition. At the outflow, do-nothing outflow conditions<sup>44</sup> are used and zero Dirichlet conditions are applied at the walls of the tube.

To capture the main physical properties of the fluid the following values are assumed. The dynamic viscosity  $\eta$  is  $1.11 \times 10^{-3}$  kg/(m s) and the constant solution density  $\rho$  equals 1100 kg/m<sup>3</sup>. The characteristic fluid velocity is 0.01 m/s and the characteristic length scale is

0.01 m. This leads, in the nondimensionalized equation, to a dimensionless viscosity  $\nu$  of  $1.01 \times 10^{-2}$ .

Only for the first two time steps, the Picard iteration was employed. As soon as two old solutions are known, the CNLE(stab) scheme can be used. With a time step length of 0.005 s, an overall time of 10 seconds was simulated. To obtain a time-averaged flow profile, a cut plane was picked in the second coil as shown in Figure 5. The velocity vectors were stored for points which are uniformly distributed across the cut plane. In a post-processing step, the arithmetic mean of each velocity component was computed at each such evaluation point over time. The time span for this averaging process ranges from 2 to 10 s.

For the finite element discretization the popular  $P_2/P_1$  Taylor-Hood pair of finite elements was chosen which uses elementwise quadratic, continuous functions for the discrete velocity and elementwise linear, continuous functions for the discrete pressure. With three velocity components and the pressure, this discretization gives rise to a linear equation system with approximately 5,600,000 degrees of freedom. Given the relative broad bandwidth which a finite element matrix exhibits in 3D, solving this problem with a sequential direct solver is not practicable. Among iterative solvers, only a few methods are applicable to this saddle point system. An iterative method with a geometric multigrid preconditioner usually shows good results in academic examples.<sup>46</sup> Here, its application is not possible due to the complicated geometry, which does not allow for a grid hierarchy. Since these standard solvers are not applicable, a parallel implementation was employed. In numerical studies presented by Wilbrandt et al.,<sup>43</sup> a flexible GMRES method<sup>47</sup> with a so-called least square commutator (LSC) preconditioner<sup>48</sup> provided by the library PETSc<sup>49</sup> was found to be a much more efficient solver

in this situation than a parallel sparse direct solver. This iterative method was used for the simulations.

The simulation was performed on a HP BL460c workstation, equipped with two 14 core Intel Xeon Sockets with 2600 Mhz clock rate. The code used to perform the simulation is the in-house finite element package ParMooN.<sup>43</sup> The computational domain was partitioned among 24 MPI processes by the graph partitioning tool Metis.<sup>50</sup> With this setup, the average solution time for one linear system of equations was about 100 s. Hence, the simulation of 10 s, i.e. 2000 time steps, took 2.75 days.

### 3. RESULTS AND DISCUSSION

**3.1 Residence Time of the Fluid Phase.** In preliminary experiments at room temperature, the conductivity signal was measured for 10 different samples of known concentration. The concentrations covered the measurement range of the conductivity probe (see Subsection 2.5). A second order polynomial was fitted to the measurement data applying the method of least squares. The measured conductivity  $\chi$  in S/m is

$$\chi = 3.6 \times 10^{-2}w - 1.5 \times 10^{-4}w^2 \quad (7)$$

where  $w$  is given in g of hydrate/kg of free water. The variance estimate is 0.004 S<sup>2</sup>/m<sup>2</sup>. Equation 7 is used to calculate the concentrations from measured conductivities in the following figures.

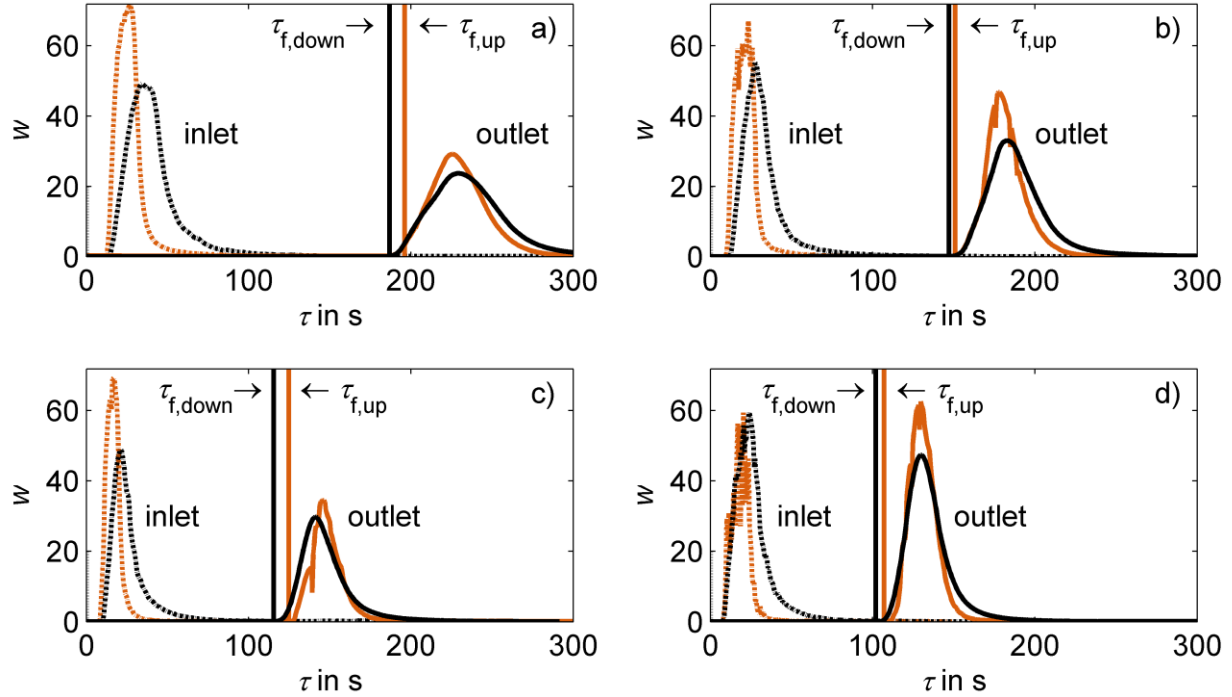


**Figure 6.** Fluid residence time for average fluid velocities according to weighing measurements of a) 0.18 m/s, b) 0.24 m/s, c) 0.29 m/s and d) 0.34 m/s. The mass fraction  $w$  is given in g hydrate/kg free water. Orange: upwards coiled HCT, black: downwards coiled HCT. Dotted curve: inlet signal at seed addition position determined by conductivity measurements, solid curve: outlet signal at Qicpic position determined by conductivity measurements, solid vertical line: average residence time determined by Coriolis type direct mass flow sensor measurements.

In Figure 6, exemplary concentration line graphs are shown for four different fluid velocities. The conductivity represented by the dotted lines was measured at the seed addition position (4) as shown in the setup in Figure 3 and can be interpreted as an inlet signal. The data represented by a solid line was recorded at the Qicpic position (6) and represents an outlet signal. With an increasing mass flow rate, the average fluid velocity increases, thus the residence time decreases and as expected the concentration arrives at the outlet earlier. Furthermore, the peak of the graphs in Figure 6a,b,d increases and the residence time range narrows for increasing fluid velocity. For comparison, the response signal for a shorter inlet pulse is illustrated in Figure 6c.

The maximum of the response signal is lower than in Figure 6b since less conductive solution was fed. The vertical lines represent the mean fluid residence time calculated from mass flow measurements of the Coriolis type direct mass flow sensor which was presented in Subsection 2.4. Weighing measurements at the corresponding pump speeds at upwards coiling resulted in average fluid velocities for water of 0.18, 0.24, 0.29 and 0.34 m/s. Comparing the upwards with downwards coiled experiments, the mean fluid residence time is slightly shorter for the downwards coiled experiments which might result from a lower pressure drop. In all diagrams, the vertical lines are located at the beginning of the outlet signals. Additionally, the response signal is much broader than the inlet signal. Hence, there is a considerable amount of dispersion in the fluid phase. For the upwards coiled experiments in orange, the noise increases with pump speed since the pump draws more air and air bubbles disturb the measurement. Consequently, a debubbler was implemented for the experiments with downwards coiling at position (3) in the setup (see Figure 3). The black curves indicate that air bubbles had been successfully removed since fewer fluctuations are present. The debubbler works like a hold-up; therefore, the response curves broaden when the debubbler is in place. The orange upwards inlet pulses without debubbler increase and decrease sharply compared with the downwards coiling inlet pulses with debubbler. Although slightly more solution is fed in downwards coiling, there is just a moderate difference for the outlet signals. Thus, the dispersion is slightly lower for downwards coiling.

All in all, fluid residence times are similar for both types of coiling and there is a considerable amount of fluid dispersion. The debubbler successfully removes irregular flow disturbances by air bubbles.

**3.2 Isothermal, i.e. Growth-Free, Potash Alum Experiments.** For low fluid velocity, Figure 7 illustrates that all crystals are slower than the average fluid. A size-dependent residence time can be observed where large crystals are faster.

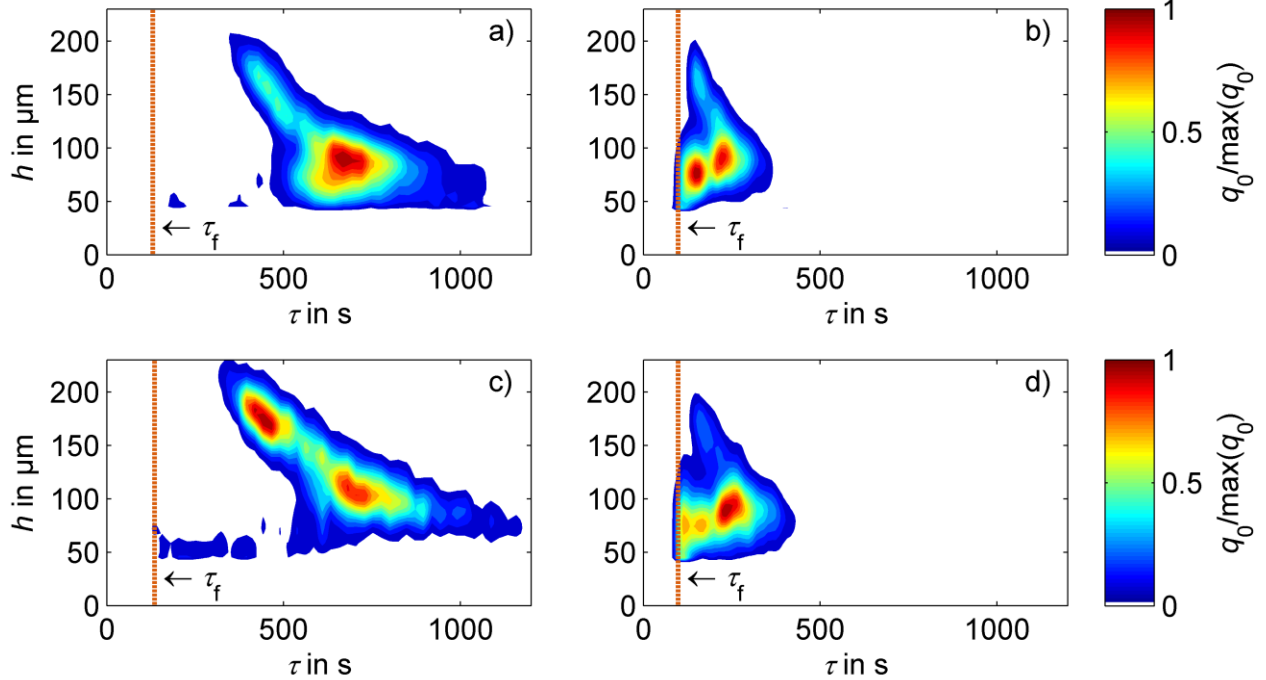


**Figure 7.** Potash alum crystal number density distribution over residence time and orthogonal distance from center to faces of the octahedron. Parts a to d depict different coiling orientations and average fluid velocities: a) upwards, 0.24 m/s, b) upwards, 0.35 m/s, c) downwards, 0.24 m/s, d) downwards, 0.35 m/s. Each figure represents the average of 7 to 14 single experiments under isothermal conditions. For each of the experiments one of the fractions presented in Figure 2 in Subsection 2.3 was applied as inlet fraction. The vertical line depicts the mean fluid residence time  $\tau_f$ .

In Figure 7b for high fluid velocity, the crystals' residence time is much lower and it nearly equals the mean fluid residence time. Again, the slowest large crystals are faster than the slowest small crystals, but overall the size-dependent separation effect vanishes. For both fluid velocities

which were stated in Subsection 2.5, there is large residence time dispersion for small particles. All in all, there is a separation by size where large crystals are moving faster.

The experiments have a final number density distribution with regard to size which is similar to the initial distribution displayed in Figure 8. The congruence confirms that the isothermal experiments were conducted at the saturation temperature and that no significant growth and dissolution were observed. The matching distributions are exemplarily shown in Figure 8 for the isothermal experiments at high fluid velocity and upwards coiling (see Figure 7b). In Subsection 2.5, it was explained that the saturation concentration of the feed solution in the reservoir was influenced by cleaning water. Therefore, small deviations between operation temperature and saturation temperature were expected. The deviations led only to minor growth (see Figure 7c) or dissolution (see Figure 7b,e) in some experiments, but overall the size range of the distribution and the peak width remained constant. The peak height decreased in all isothermal experiments compared to the initial seed fraction since nuclei appeared. The nuclei were possibly originating from initial breeding induced by the nontreated dry seeds (see Subsection 2.3). This assumption is supported by the observation that the nuclei arrive at the HCT outlet in Figure 7 between the average fluid and the crystal residence time. For the residence time plots in Figure 7, the small crystals below the minimal size defined in Subsection 2.3 were not taken into account since the location of nucleation may differ from the seed addition position. The separation of nuclei and the grown seed crystals by the imaging algorithm was explained in Subsection 2.2.

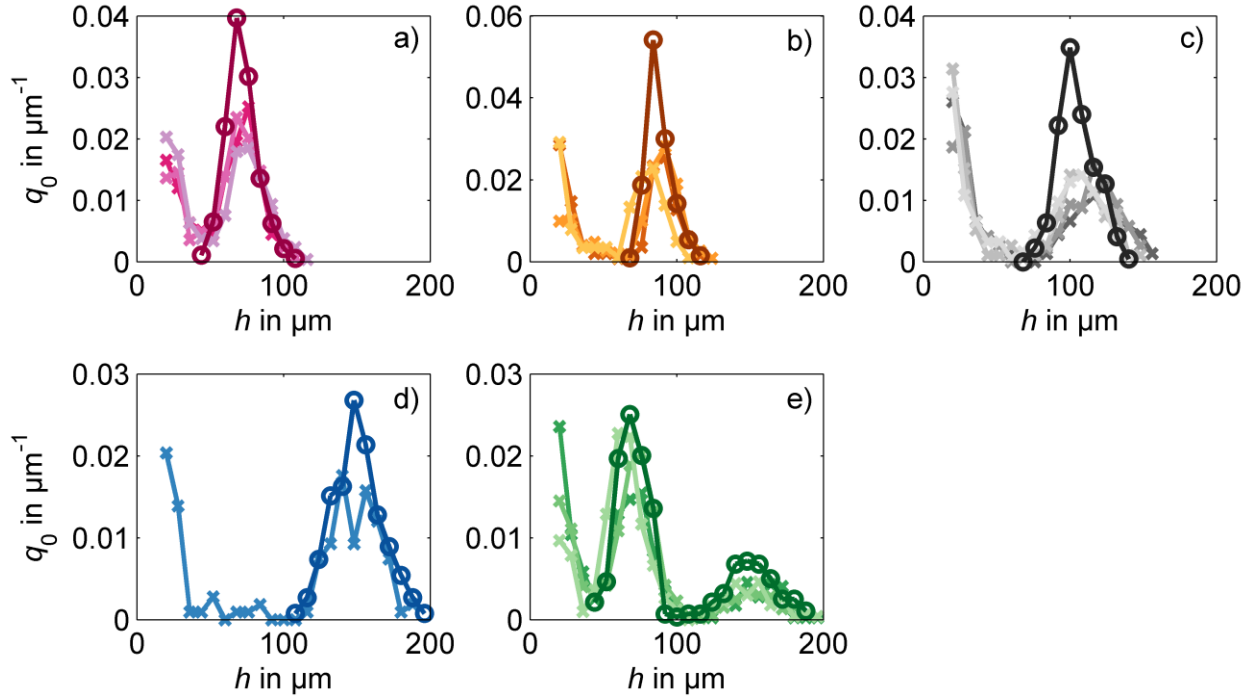


**Figure 8.** Number density distribution over crystal size  $h$  for the initial distribution analyzed by experiments in anti-solvent from Figure 2 (dark curves with circular markers o) and for the isothermal experiments in potash alum solution from Figure 7b (lighter curves with cross markers  $\times$ ) for the different size fractions: a) A, b) B, c) C, d) D, e) A+D.

**3.3 Crystal Growth in the HCT.** Growth experiments were conducted as described in Subsection 2.5 for all inlet size fractions as shown in Figure 2, for at least two different supersaturation ratios and for all combinations of low and high fluid velocity and upward/downward fluid flow. In all experiments, growth increased with saturation as expected. Exemplarily, results are given for upwards coiling at a low fluid velocity. For this setup, the largest residence times and consequently the largest absolute crystal growth are reached. In Figure 9, the number density distributions are shown for a mix (A+D) of the smallest size fraction (A) and the largest one (D) as described in Subsection 2.3. Due to small seed amounts (approximately 100 mg of the small fraction and 200 mg of the large fraction), it is assumed that

changes in concentration are negligible. Therefore, the supersaturation ratio was calculated for the known inlet concentration applying the measured temperatures.

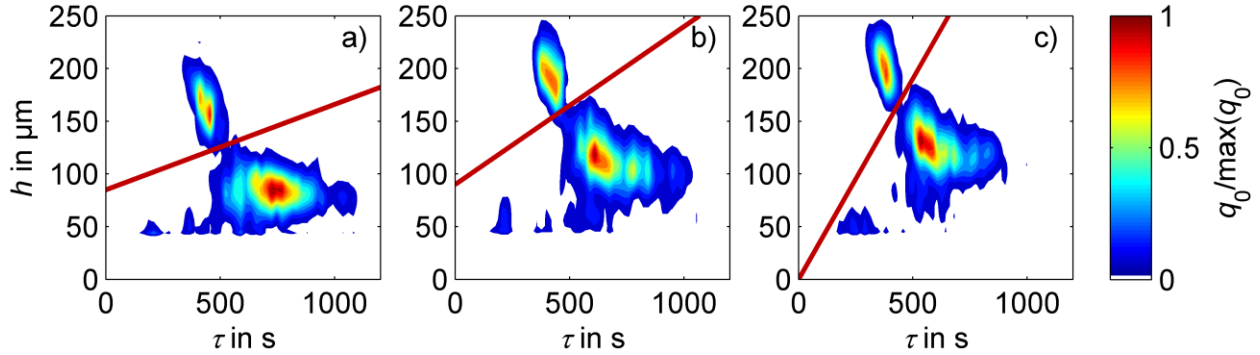


**Figure 9.** Normalized number density distribution over residence time and crystal size for potash alum crystals measured at the HCT outlet. The HCT is operated at an average fluid velocity of 0.24 m/s and coiled upwards. The outlet supersaturation ratio increases from part a to c: a)  $S_{out}=1.02$ , b)  $S_{out}=1.11$ , c)  $S_{out}=1.15$ . The inlet seed fraction is a mix (A+D) of the smallest sieved size fraction and the largest one presented in Figure 2 in Subsection 2.3. The red lines are introduced to separate the large crystal fraction (D) from the small one (A).

In Figure 9, crystal size increases and residence time decreases with outlet supersaturation. For considering the large fraction and the small one separately for the mixed fractions, the crystal size distributions are separated and divided in two regions, shown by red lines in Figure 9. Large and small crystals had size-dependent residence times. Therefore, it had to be reviewed whether there were variations over time influencing crystal growth. During each of the three experiments, the inlet and outlet temperature were approximately constant and the resulting supersaturation ratio varied by a maximum of 0.014. Consequently, it can be assumed that all crystal sizes were exposed to approximately the same supersaturation profile. In case of mass depletion in the continuous phase, the high mean fluid velocity and the slow velocity of the small crystals led to a constant feed of the crystals with fresh solution. Since small crystals remain in the HCT longer,

they have more time to grow than large crystals. Therefore, the residence time distribution in the HCT supports a narrowing effect on the CSSD. Nevertheless, for all three experiments, the difference between the large fraction and the small fraction mean sizes remained approximately constant. This behavior was probably caused by a residence time dispersion of the small crystals which is discussed further at the end of this subsection. As a conclusion, a clear narrowing effect on the CSSD was not observed, albeit the width of the CSSD remained constant.

**Table 1:** HCT inlet and outlet supersaturation for different experiments are sorted by outlet supersaturation ratio from high to low.

Label	Size fraction	$S_{\text{in}}$	$S_{\text{out}}$
1	large	0.95	1.21
2	large	0.93	1.20
3	mixed	0.93	1.15
4	small	0.94	1.15
5	small	0.90	1.14
6	mixed	0.91	1.11
7	small	0.98	1.04
8	large	0.96	1.03
9	large	0.96	1.02
10	mixed	0.96	1.02
11	large	0.96	1.01
12	small	0.96	1.01

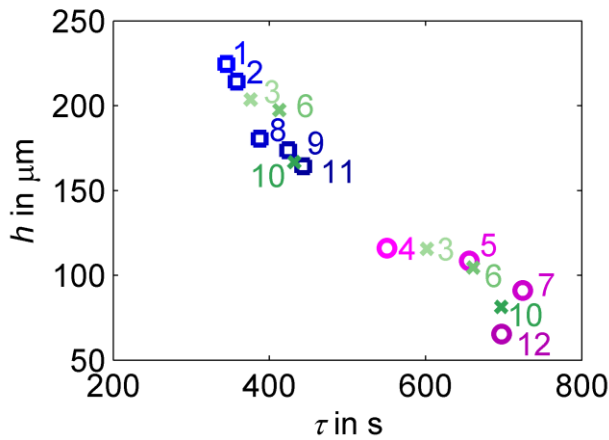


**Figure 10.** Mean crystal size and mean residence time are illustrated for the experiments listed in Table 1. The HCT outlet supersaturation ratio decreases with increasing experiment number. Experiments with large crystal size fractions (D) are shown as blue squares, small fractions (A) as magenta spheres and the large and small fractions of the mixed experiments (A+D) as green crosses.

Preliminary experiments indicated that slight variations in the inlet saturation have only a small effect on the final CSSD compared with the outlet supersaturation ratio. In Table 1, experiments are listed for decreasing outlet supersaturation ratio. The mixed experiments which were presented in Figure 9 are included in Figure 10 and Table 1. In Figure 10, the final mean crystal size increases with increasing supersaturation while the mean residence decreases with increasing supersaturation as expected. Considering residence time, all markers follow the same trend with slight deviations for the small fraction. This deviation in Figure 10 could be explained by the broad RTD of small crystals which was depicted in Figure 9. Comparing the large fraction of the mixed (3, 6, 9) with the separate experiments (1, 2, 8, 9, 11), the mean values follow the same trend. Comparing the small fraction mean values of the mixed (3, 6, 9) with the separate experiments (4, 5, 7, 12), there is also no deviating trend. Therefore, the mixing of the large and

the small crystal fraction does not affect the residence time. Thus, the particle-particle interactions of different size fractions are not considered as primary cause for the size-dependent separation in the tube.

In the following, the results of the growth experiments are interpreted with regard to crystal growth rate dispersion (GRD). GRD of potash alum crystal populations was observed in batch,<sup>39</sup> flow-cell<sup>51</sup> and MSMPR<sup>52</sup> experiments. The effect of GRD is analyzed on the basis of the mixed experiments 3, 6 and 10 (see Table 1, Figures 9 and 10). The distance of the mean sizes of the large and small fraction is 88, 93 and 85 µm and remains approximately constant. Srisanga et al.<sup>53</sup> analyzed the GRD for bimodal distributions which are exposed to equal conditions. For the bimodal distributions, the distance of the distributions' peaks remains constant while the distributions broaden and the mode decreases. In case of the HCT, small crystals have a higher residence time and more time to grow. Assuming that the crystals were subject to similar conditions, the small crystals should approach the large crystals and the distance of the modes of the small and the large fraction should decrease, but this is not observed in the experiments in the HCT as mentioned in the beginning of this subsection. The experimental observations might be explained by nuclei or dust particles from initial breeding which are visible at the bottom in Figure 9. They are just slightly smaller than the analyzed crystals at the HCT outlet and reduce the mean value of the grown small size fraction. Tanneberger et al.<sup>52</sup> observed smaller growth rates for very small crystals in the size range of up to 60 µm compared to larger crystals of 500 µm size. The size range of their crystals is slightly larger but still similar to the crystal sizes in this work. Therefore, their observation might explain why the size peaks stay the same distance apart in this work.

In general, the effect of GRD on the distributions should increase from experiment 10 to 3 in Figures 9 and 10. A significant broadening of the distributions in  $h$ -direction cannot be observed and the standard deviation does not increase. The effect of GRD is difficult to estimate for the present experiments since it differs from isothermal, non-nucleating ideal model experiments with crystals of identical residence time and history. All in all, a major effect of GRD on the potash alum crystal population in the HCT setup is not recognizable.

Growth was realized for systematic parameter variations in the HCT for a large number of experiments without tube clogging. The width of the CSSD remained constant during the experiments with mixed fractions. A mixing effect on the crystal residence time could not be observed. Consequently, the size-dependent residence time cannot be contributed to particle-particle interactions of crystals with different size.

**3.4 Size-Dependent Particle Residence Time in the HCT.** A separation effect by crystal size was observed in the HCT in Subsections 3.2 and 3.3. Large potash alum crystals had a shorter residence time than small particles. In the following, possible reasons are discussed and their contributions to the effect are estimated.

In general, particle-fluid interaction, particle-particle interaction and particle-wall interaction may influence the particle residence time. Considering particle-fluid interaction, particle rotation is part of angular momentum balances and particle forces are included in momentum balances. In these models and in simulations, particles are usually modeled as spheres. The octahedral crystal shape of potash alum might be responsible for size separation. According to Haider and Levenspiel,<sup>54</sup> the sphericity of an octahedron is 0.85 whereas it is 1 for a sphere. In the Stokes

regime, the small non-sphericity leads only to small deviations from the spherical drag coefficient. Therefore, the crystal shape is not investigated further in this work.

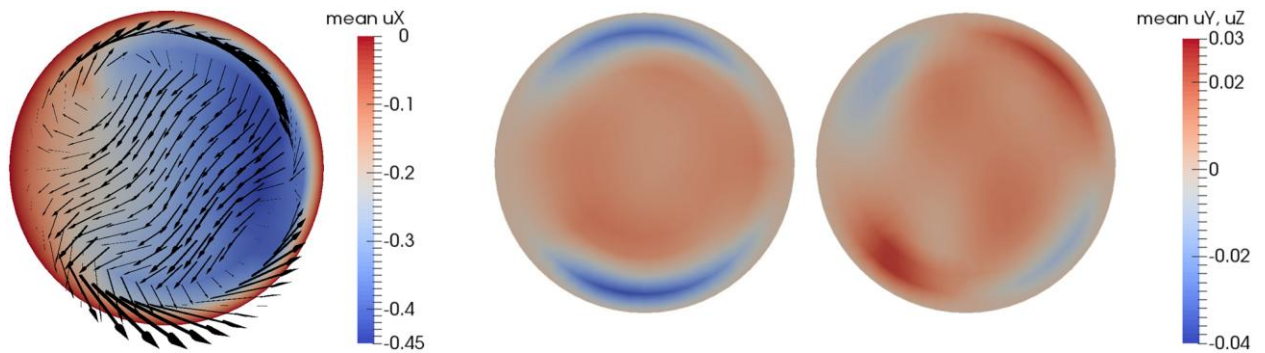
An additional idea to explain the residence time behavior is that large particles are transported on top of a bed of small particles. In Subsection 3.3, the residence time of crystals in mixed experiments was compared with separate experiments and resulted to be similar. Therefore, the mixing behavior is not identified as the main cause.

During the experiments, it was visually observed that the particles were located near the tube bottom. Thus, it can be suggested that all particles are subject to similar drag forces. The fluid velocity at the bottom wall is zero. Since the center and the reference area of larger crystals are located in an area of higher fluid velocities, a shorter residence time may result for larger crystals and explain the size-dependent residence time behavior. The presumption of small-scale flow characteristics is fostered by a rough calculation which yields a Reynolds number, based on the average fluid velocity, the diameter of the pipe, and the properties of the fluid, of approximately 1280 for the flow field. This is not yet a turbulent regime, but complex time-dependent flow structures can already develop. For higher Reynolds numbers of approximately 1820 in the transient region, the separation effect diminished in the experiments. This favors the assumption that the flow field in the HCT crystallizer develops micro structures which the smaller crystals follow while the inert larger crystals follow only the main flow direction through the tube.

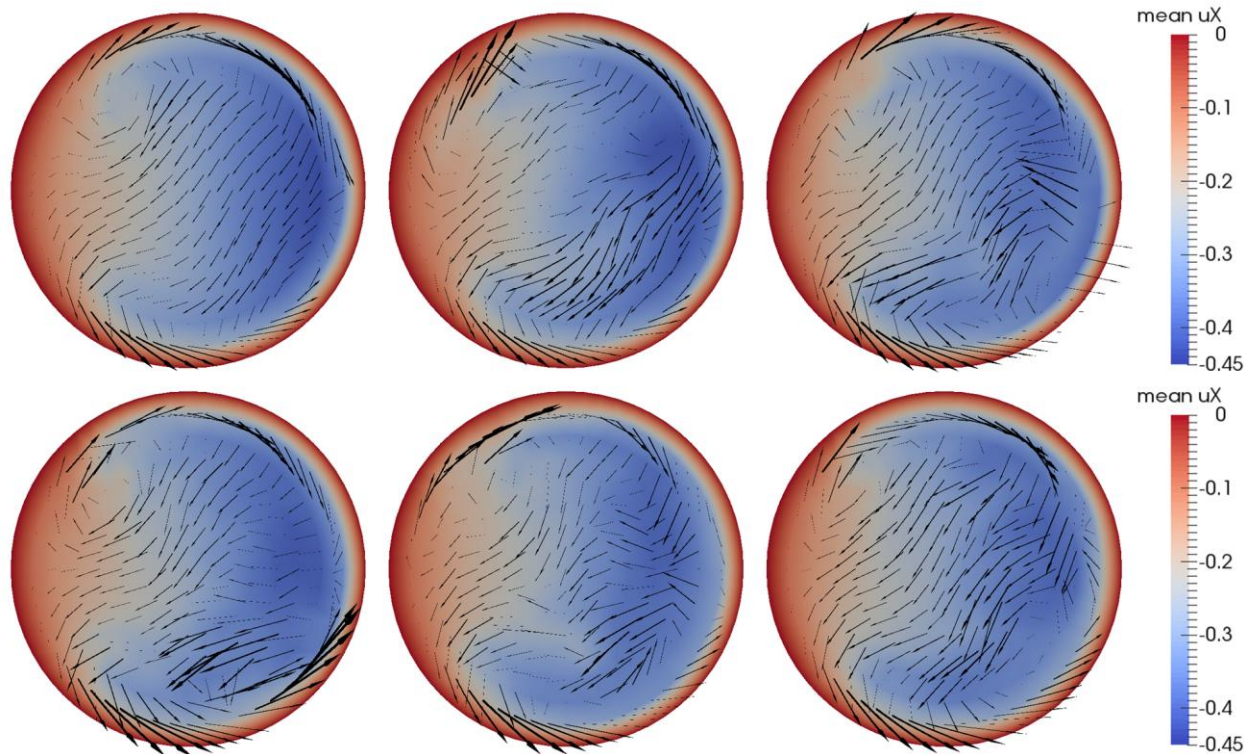
**3.5 Flow Field Simulation Results.** The numerical and computational methods which were applied for the flow field simulations in this work are presented in Subsection 2.7 and the simulation results are shown in this subsection. In a post-processing step, the time average of the velocity field has been computed at a certain cut-plane through the tube which was depicted in

Figure 5. This time average can be used as an input flow field for further particle movement simulations. This way, time-consuming simulations of the complex flow field are avoided. The result of the time averaging process at the chosen cut plane is depicted in Figure 11.

The time-averaged velocity field shows that the peak in flow direction is shifted towards the outer wall (with respect to the helix). A secondary flow of considerably less strength than the main flow can be observed with two vortices that transport the fluid from the outer wall through the center of the pipe to the inner wall and then along the wall back to the outer wall. This secondary flow is not symmetric; the lower vortex is somewhat larger than the upper vortex. Nevertheless, the mean field resembles the so-called Dean vortices that are known for flows in curved pipes, e.g., see Berger et al.<sup>55</sup> In fact, since the increase in elevation of the helix is small compared with the radius of its coil as stated in Subsection 2.6, some similarity to a flow field in a curved pipe should be expected. The main difference to the secondary flow in curved pipes as discussed by Berger et al.<sup>55</sup> is the non-symmetry of the secondary flow field.



**Figure 11.** The average velocity in m/s at the cut plane in Figure 5 is presented;  $x$ -,  $y$ - and  $z$ -component from left to right. Averaging was performed in the time interval [2 s, 10 s]. The outer wall of the coil is located in the positive  $y$ -direction at the right side of the figures.



**Figure 12.** The velocity solution in m/s is shown at times 2.435, 3.255, 5.965, 6.620, 8.395, 9.975 s in the cut plane illustrated in Figure 5. Coloring is according to the  $x$ -component, the black arrows show the  $y$ - and the  $z$ -component. The outer wall of the coil is located in the positive  $y$ -direction at the right side of the figures.

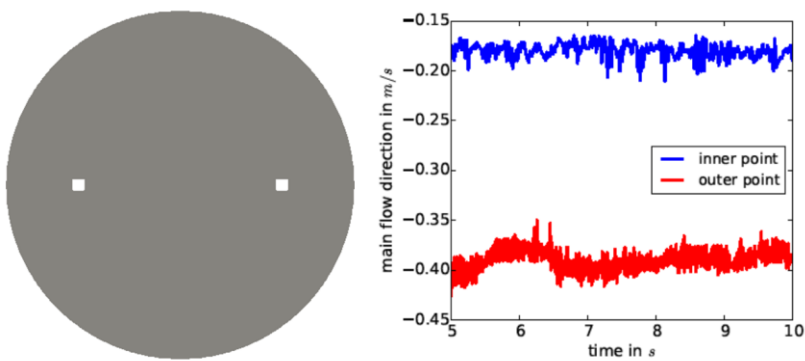


**Figure 13.** Temporal evolution of the velocity in main flow direction in two points in the cut plane depicted in Figure 5. The left point (related to the blue line) is close to the interior wall of the coil and the right point (related to the red line) close to its outer wall.

The Reynolds numbers in this work, as stated in Subsection 3.4, are in the laminar flow regime following the transition criterion used by Piazza and Ciofalo.<sup>56</sup> Snapshots of the flow field at the cut plane depicted in Figure 5 reveal that the flow is indeed time-dependent, see Figure 12. The flow is by far less regular than its mean. Thus, one can conclude from these pictures that a considerable mixing of the secondary flow occurs. The instationarity of the flow field can be observed as well in Figure 13 where the evolution of the velocity in mean flow direction in two points within the pipe is depicted.

Altogether, one can imagine the path of particles that move along the mean secondary flow as a helix within the pipe, either on its lower or on its upper part. Consequently, the length of such a path is much longer than the path length of a particle that moves only along the main flow direction. Since the strength of the secondary flow is quite small, compared with the mean flow, it can be expected that primarily small particles are affected by the secondary flow and thus take longer paths. Since the paths are longer and the secondary flow occurs also in parts of the pipe with lower velocity in main direction, it can be expected that these particles posses a longer residence time compared with particles that move along the main flow direction in a vicinity of the region with the peak flow. Figure 13 shows clearly that there is a big difference of the velocity in main direction between locations closer to the outer and the inner wall of the coil. The impact of the mixing of the secondary flow on paths of particles is a topic of further research.

#### 4. CONCLUSION

A principal finding of this work is that potash alum crystals show a size-dependent residence time in the HCT which leads to particle separation. The main reason for this separation has not yet been identified in literature. Palazoglu and Sandeep<sup>32</sup> found effects on the particle residence

time when mixing particles of different density in a HCT but did not investigate the particle size dependency. In this study, experiments indicated that the size-dependent residence time was not caused by the mixing of different size fractions. These observations led to the hypothesis that small flow structures might exist which possess a larger impact on small particles than on large ones and cause a longer residence time of small particles. To support this hypothesis, a direct numerical simulation of the flow in a representative part of the HCT was performed. In fact, a time-dependent secondary flow was observed, whose temporal mean pattern shows two vortices. Along such vortices, small particles can be transported to regions with a slow flow in main direction. Detailed numerical studies of the particle behavior in such flow fields will be part of our future research.

For the potash alum-water model system in an upwards-coiled HCT of 34 m length under an average fluid velocity of 0.24 m/s, small crystals of a mean size of 81  $\mu\text{m}$  had a mean residence time of 670 s and larger crystals of about 167  $\mu\text{m}$  had a shorter mean residence time of about 430 s. Applying a high supersaturation at the HCT outlet of 1.15, the mean size increased by 35  $\mu\text{m}$  for the small crystals and by a similar value of 37  $\mu\text{m}$  for the large crystals and the distribution widths remained constant.

The crystal residence time determines the time for them to grow. When the RTD is not uniform for all crystal sizes, the crystal size and shape distribution (CSSD) changes. Provided that small crystals are slower, they have more time to grow. Therefore, the HCT can potentially narrow the CSSD during the growth. This is an important advantage in comparison to other continuous crystallizers as MSMPRs or cascades of MSMPRs. The continuous CFI is characterized by the best mixing properties of tubular crystallizers. However, the size-dependent residence time distribution in the HCT can be advantageous with respect to crystal growth. The

distribution width remained constant during the growth experiments in this study. All in all, the HCT presented in this work is a suitable device to grow crystals of a desired size and shape distribution.

Under industrial conditions, higher suspension densities and continuous feeding of seed crystals are applied. In this case, similar supersaturation levels can be reached by stronger cooling. Here, it was found that the crystal residence times exceed the mean fluid residence time especially for small crystals. This is an advantage to narrow the CSSD since small crystals stay longer inside the system and can grow larger correspondingly.

In conclusion, CSSD control and continuous crystallization were combined in this study. The Qicpic-based shape estimation methods used for potash alum in this work have already been applied to bivariate crystal populations in a batch crystallizer.<sup>57</sup> Hence, future research should apply shape control to bivariate populations in HCTs of different temperatures to reach a desired final CSSD.

## ASSOCIATED CONTENT

**Supporting Information.** The Supporting Information is available free of charge on the ACS Publications website at <http://pubs.acs.org>.

Equilibrium solubility, and details on a Gaussian kernel density estimator for plot generation.

## AUTHOR INFORMATION

### Corresponding Author

\*Phone: +49 (0)391 6754636. Fax: +49 (0)391 6711245. Email: viktoria.wiedmeyer@ovgu.de

## **Author Contributions**

The manuscript was written through contributions of all authors. All authors have given approval to the final version of the manuscript.

## **Notes**

The authors declare no competing financial interest.

## **ACKNOWLEDGMENT**

We like to thank two unknown reviewers whose suggestions greatly helped to improve this paper.

The financial support of the DFG (Deutsche Forschungsgemeinschaft) within the priority program SPP 1679 "Dynamic simulation of interconnected solids processes DYNSIM-FP" under the grant numbers JO 329/10-2 and SU 189/6-2 is gratefully acknowledged.

## **ABBREVIATIONS**

API, active pharmaceutical ingredient; CFI, coiled flow inverter; CNLE(stab), linearly extrapolated Crank-Nicolson; CSSD, crystal size and shape distribution; DNS, direct numerical simulation; FEM, finite element method; GRD, growth rate dispersion; HCT, helically-coiled flow tube; IMEX, implicit-explicit; LSC, least square commutator; MSMPR, mixed-suspension, mixed-product-removal; RTD, residence time distribution.

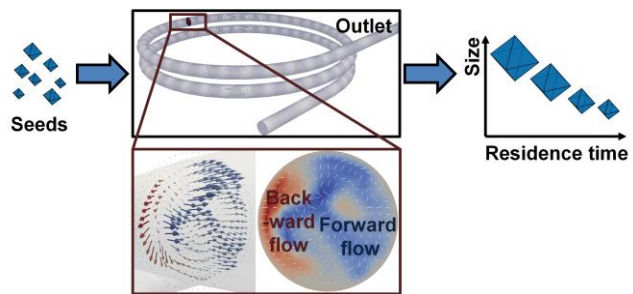
## **REFERENCES**

- (1) ter Horst, J. H.; Schmidt, C.; Ulrich, J. Fundamentals of Industrial Crystallization. In *Handbook of Crystal Growth*, 2nd ed.; Rudolph, P., Ed. Elsevier: Boston, 2015; pp 1317-1349.
- (2) Lovette, M. A.; Browning, A. R.; Griffin, D. W.; Sizemore, J. P.; Snyder, R. C.; Doherty, M. F. Crystal Shape Engineering. *Ind. Eng. Chem. Res.* **2008**, *47*, 9812-9833.

- (3) Kircher, M.; Pfefferle, W. The fermentative production of l-lysine as an animal feed additive. *Chemosphere* **2001**, *43*, 27-31.
- (4) Mullin, J. W. Crystallization and Precipitation. In *Ullmann's Encyclopedia of Industrial Chemistry*, Wiley-VCH: Weinheim, 2003.
- (5) Jones, A. G.; Mydlarz, J. Slurry filtrability of potash alum. *Can. J. Chem. Eng.* **1990**, *68*, 513-518.
- (6) Variankaval, N.; Cote, A. S.; Doherty, M. F. From form to function: Crystallization of active pharmaceutical ingredients. *AIChE J.* **2008**, *54*, 1682-1688.
- (7) Yang, H. G.; Sun, C. H.; Qiao, S. Z.; Zou, J.; Liu, G.; Smith, S. C.; Cheng, H. M.; Lu, G. Q. Anatase TiO<sub>2</sub> single crystals with a large percentage of reactive facets. *Nature* **2008**, *453*, 638-641.
- (8) Mullin, J. W. *Crystallization*; 4th ed.; Butterworth-Heinemann: Oxford, 2001.
- (9) Gottlieb, O. High Containment in der pharmazeutischen Industrie. *Proc. TechnoPharm* **2016**, *6*, 26-33.
- (10) Li, J.; Trout, B. L.; Myerson, A. S. Multistage Continuous Mixed-Suspension, Mixed-Product Removal (MSMPR) Crystallization with Solids Recycle. *Org. Process Res. Dev.* **2016**, *20*, 510-516.
- (11) Klutz, S.; Kurt, S. K.; Lobedann, M.; Kockmann, N. Narrow residence time distribution in tubular reactor concept for Reynolds number range of 10–100. *Chem. Eng. Res. Des.* **2015**, *95*, 22-33.
- (12) Jiang, M.; Papageorgiou, C. D.; Waetzig, J.; Hardy, A.; Langston, M.; Braatz, R. D. Indirect Ultrasonication in Continuous Slug-Flow Crystallization. *Cryst. Growth Des.* **2015**, *15*, 2486-2492.
- (13) Wong, S. Y.; Cui, Y.; Myerson, A. S. Contact Secondary Nucleation as a Means of Creating Seeds for Continuous Tubular Crystallizers. *Cryst. Growth Des.* **2013**, *13*, 2514-2521.
- (14) Vashisth, S.; Kumar, V.; Nigam, K. D. P. A review on the potential applications of curved geometries in process industry. *Ind. Eng. Chem. Res.* **2008**, *47*, 3291-3337.
- (15) Agrawal, S.; Nigam, K. D. P. Modelling of a coiled tubular chemical reactor. *Chem. Eng. J.* **2001**, *84*, 437-444.
- (16) Naphon, P.; Wongwises, S. A review of flow and heat transfer characteristics in curved tubes. *Renewable Sustainable Energy Rev.* **2006**, *10*, 463-490.
- (17) Liu, S.; Sakr, M. A comprehensive review on passive heat transfer enhancements in pipe exchangers. *Renewable Sustainable Energy Rev.* **2013**, *19*, 64-81.
- (18) Eder, R. J. P.; Schrank, S.; Besenhard, M. O.; Roblegg, E.; Gruber-Woelfler, H.; Khinast, J. G. Continuous Sonocrystallization of Acetylsalicylic Acid (ASA): Control of Crystal Size. *Cryst. Growth Des.* **2012**, *12*, 4733-4738.
- (19) Lawton, S.; Steele, G.; Shering, P.; Zhao, L.; Laird, I.; Ni, X.-W. Continuous Crystallization of Pharmaceuticals Using a Continuous Oscillatory Baffled Crystallizer. *Org. Process Res. Dev.* **2009**, *13*, 1357-1363.
- (20) Briggs, N. E. B.; Schacht, U.; Raval, V.; McGlone, T.; Sefcik, J.; Florence, A. J. Seeded Crystallization of  $\beta$ -l-Glutamic Acid in a Continuous Oscillatory Baffled Crystallizer. *Org. Process Res. Dev.* **2015**, *19*, 1903-1911.
- (21) Pionetti, F. R.; Delebecque, L. Coaxial pipe assembly including a thermally insulating sleeve. U.S. Patent 9,267,637 B2, Feb 23, 2016.

- (22) Furuta, M.; Mukai, K.; Cork, D.; Mae, K. Continuous crystallization using a sonicated tubular system for controlling particle size in an API manufacturing process. *Chem. Eng. Process.* **2016**, *102*, 210-218.
- (23) Eder, R. J. P.; Radl, S.; Schmitt, E.; Innerhofer, S.; Maier, M.; Gruber-Woelfler, H.; Khinast, J. G. Continuously Seeded, Continuously Operated Tubular Crystallizer for the Production of Active Pharmaceutical Ingredients. *Cryst. Growth Des.* **2010**, *10*, 2247-2257.
- (24) Eder, R. J. P.; Schmitt, E. K.; Grill, J.; Radl, S.; Gruber-Woelfler, H.; Khinast, J. G. Seed loading effects on the mean crystal size of acetylsalicylic acid in a continuous-flow crystallization device. *Cryst. Res. Technol.* **2011**, *46*, 227-237.
- (25) Besenhard, M. O.; Hohl, R.; Hodzic, A.; Eder, R. J. P.; Khinast, J. G. Modeling a seeded continuous crystallizer for the production of active pharmaceutical ingredients. *Cryst. Res. Technol.* **2014**, *49*, 92-108.
- (26) Besenhard, M. O.; Thurnberger, A.; Hohl, R.; Faulhammer, E.; Rattenberger, J.; Khinast, J. G. Continuous API-crystal coating via coacervation in a tubular reactor. *Int. J. Pharm.* **2014**, *475*, 198-207.
- (27) Besenhard, M. O.; Neugebauer, P.; Ho, C.-D.; Khinast, J. G. Crystal Size Control in a Continuous Tubular Crystallizer. *Cryst. Growth Des.* **2015**, *15*, 1683-1691.
- (28) Buckley, H. E. The crystallization of potash-alum and the effect of certain added impurities on its habit. *Z. Kristallogr.* **1930**, *73*, 443-464.
- (29) Borchert, C.; Temmel, E.; Eisenschmidt, H.; Lorenz, H.; Seidel-Morgenstern, A.; Sundmacher, K. Image-Based In Situ Identification of Face Specific Crystal Growth Rates from Crystal Populations. *Cryst. Growth Des.* **2014**, *14*, 952-971.
- (30) Baptista, P. N.; Oliveira, F. A. R.; Caldas, S. M.; Oliveira, J. C.; Sastry, S. K. Effect of product and process variables in the flow of spherical particles in a carrier fluid through straight tubes. *J. Food Process. Preserv.* **1996**, *20*, 467-486.
- (31) Redlinger-Pohn, J. D.; Jagiello, L. A.; Bauer, W.; Radl, S. Mechanistic understanding of size-based fiber separation in coiled tubes. *Int. J. Multiphase Flow* **2016**, *83*, 239-253.
- (32) Palazoglu, T. K.; Sandeep, K. P. Effect of tube curvature ratio on the residence time distribution of multiple particles in helical tubes. *Lebensm.-Wiss. Technol.* **2004**, *37*, 387-393.
- (33) Tiwari, P.; Antal, S. P.; Podowski, M. Z. Three-dimensional fluid mechanics of particulate two-phase flows in U-bend and helical conduits. *Phys. Fluids* **2006**, *18*, 043304.
- (34) Mullin, J. W.; Garside, J.; Unahabokha, R. Diffusivities of ammonium and potassium alums in aqueous solutions. *J. Appl. Chem.* **1965**, *15*, 502-505.
- (35) de Albuquerque, I.; Ochsenbein, D. R.; Morari, M.; Mazzotti, M. Effect of needle-like crystal shape on measured particle size distributions. *AIChE J.* **2016**, *62*, 2974-2985.
- (36) Reinhold, A.; Briesen, H. Convex Geometry for the Morphological Modeling and Characterization of Crystal Shapes. *Part. Part. Syst. Charact.* **2011**, *28*, 37-56.
- (37) Zhang, Y.; Sizemore, J. P.; Doherty, M. F. Shape evolution of 3-dimensional faceted crystals. *AIChE J.* **2006**, *52*, 1906-1915.
- (38) Gadewar, S. B.; Hofmann, H. M.; Doherty, M. F. Evolution of Crystal Shape. *Cryst. Growth Des.* **2004**, *4*, 109-112.
- (39) Girolami, M. W.; Rousseau, R. W. Size-dependent crystal growth—A manifestation of growth rate dispersion in the potassium alum-water system. *AIChE J.* **1985**, *31*, 1821-1828.

- (40) Mullin, J. W.; Sipek, M. Solubility and density isotherms for potassium aluminum sulfate-water-alcohol systems. *J. Chem. Eng. Data* **1981**, *26*, 164-165.
- (41) Sang-II Kwon, J.; Nayhouse, M.; Orkoulas, G.; Christofides, P. D. Crystal shape and size control using a plug flow crystallization configuration. *Chem. Eng. Sci.* **2014**, *119*, 30-39.
- (42) Barrett, P.; Glennon, B. Characterizing the Metastable Zone Width and Solubility Curve Using Lasentec FBRM and PVM. *Chem. Eng. Res. Des.* **2002**, *80*, 799-805.
- (43) Wilbrandt, U.; Bartsch, C.; Ahmed, N.; Alia, N.; Anker, F.; Blank, L.; Caiazzo, A.; Ganeshan, S.; Giere, S.; Matthies, G.; Meesala, R.; Shamim, A.; Venkatesan, J.; John, V. ParMooN—A modernized program package based on mapped finite elements. *Comput. Math. Appl.* **2017**, DOI: 10.1016/j.camwa.2016.12.020.
- (44) John, V. *Finite Element Methods for Incompressible Flow Problems*; Springer Series in Computational Mathematics 51; Springer-Verlag: Berlin, 2016.
- (45) Ingram, R. A new linearly extrapolated crank-nicolson time-stepping scheme for the navier-stokes equations. *Math. Comput.* **2013**, *82*, 1953-1973.
- (46) John, V. On the efficiency of linearization schemes and coupled multigrid methods in the simulation of a 3D flow around a cylinder. *Int. J. Numer. Methods Fluids* **2006**, *50*, 845-862.
- (47) Saad, Y. A Flexible Inner-Outer Preconditioned GMRES Algorithm. *SIAM J. Sci. Comput.* **1993**, *14*, 461-469.
- (48) Elman, H. C.; Silvester, D. J.; Wathen, A. J. *Finite Elements and Fast Iterative Solvers: with Applications in Incompressible Fluid Dynamics*; 2nd ed.; Oxford University Press: Oxford, 2014.
- (49) Balay, S.; Abhyankar, S.; Adams, M. F.; Brown, J.; Brune, P.; Buschelman, K.; Dalcin, L.; Eijkhout, V.; Gropp, W. D.; Kaushik, D.; Knepley, M. G.; McInnes, L. C.; Rupp, K.; Smith, B. F.; Zampini, S.; Zhang, H.; Zhang, H. *PETSc Users Manual*; Argonne National Laboratory: 2016.
- (50) Karypis, G.; Kumar, V. A Fast and High Quality Multilevel Scheme for Partitioning Irregular Graphs. *SIAM J. Sci. Comput.* **1998**, *20*, 359-392.
- (51) Wang, S.; Mersmann, A.; Kind, M. Verification of the constant crystal growth model for attrition particles and its relevance to the modeling of crystallizers. *J. Cryst. Growth* **1990**, *99*, 1104-1107.
- (52) Tanneberger, U.; Lacmann, R.; Herden, A.; Klapper, H.; Schmiemann, D.; Becker, R. A.; Mersmann, A.; Zacher, U. The dispersion of growth rate as a result of different crystal perfection. *J. Cryst. Growth* **1996**, *166*, 1074-1077.
- (53) Srisanga, S.; Flood, A. E.; Galbraith, S. C.; Rugmai, S.; Soontaranon, S.; Ulrich, J. Crystal Growth Rate Dispersion versus Size-Dependent Crystal Growth: Appropriate Modeling for Crystallization Processes. *Cryst. Growth Des.* **2015**, *15*, 2330-2336.
- (54) Haider, A.; Levenspiel, O. Drag coefficient and terminal velocity of spherical and nonspherical particles. *Powder Technol.* **1989**, *58*, 63-70.
- (55) Berger, S. A.; Talbot, L.; Yao, L. S. Flow in curved pipes. *Annu. Rev. Fluid Mech.* **1983**, *15*, 461-512.
- (56) Piazza, I. D.; Ciofalo, M. Transition to turbulence in toroidal pipes. *J. Fluid Mech.* **2011**, *687*, 72-117.
- (57) Eisenschmidt, H.; Bajcinca, N.; Sundmacher, K. Optimal Control of Crystal Shapes in Batch Crystallization Experiments by Growth-Dissolution Cycles. *Cryst. Growth Des.* **2016**, *16*, 3297-3306.



For Table of Contents Only